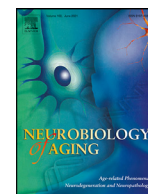




Contents lists available at ScienceDirect

Neurobiology of Aging

journal homepage: www.elsevier.com/locate/neuaging.org

Association of longitudinal cognitive decline with diffusion MRI in Gray Matter, Amyloid, and Tau deposition

Wei-en Wang^{a,g}, Rob Chen^b, Robin Perry Mayrand^{c,g}, Malek Adjouadi^{c,g}, Ruogu Fang^{b,f}, Steven T. DeKosky^{d,g}, Ranjan Duara^{e,g}, Stephen A. Coombes^{a,g}, David E. Vaillancourt^{a,b,d,f,g,*}, for the Alzheimer's Disease Neuroimaging Initiative¹

^a Department of Applied Physiology and Kinesiology, University of Florida, Gainesville, FL, USA

^b J. Crayton Pruitt Family Department of Biomedical Engineering, University of Florida, Gainesville, FL, USA

^c Center for Advanced Technology and Education, Department of Electrical and Computer Engineering, Florida International University, Miami, FL, USA

^d Department of Neurology, University of Florida, Gainesville, FL, USA

^e Wein Center for Alzheimer's Disease and Memory Disorders, Mount Sinai Medical Center, Miami Beach, FL, USA

^f Center for Cognitive Aging and Memory, McKnight Brain Institute, University of Florida, Gainesville, FL, USA

^g 1Florida Alzheimer's Disease Research Center (ADRC), University of Florida, Gainesville, FL, USA

ARTICLE INFO

Article history:

Received 25 January 2022

Revised 21 October 2022

Accepted 25 October 2022

Available online 5 November 2022

Keywords:

Diffusion MRI

Alzheimer's disease

Free-water imaging

Amyloid

Tau

Positron emission tomography

Machine learning

ABSTRACT

Extracellular amyloid plaques in gray matter are the earliest pathological marker for Alzheimer's disease (AD), followed by abnormal tau protein accumulation. The link between diffusion changes in gray matter, amyloid and tau pathology, and cognitive decline is not well understood. We first performed cross-sectional analyses on T1-weighted imaging, diffusion MRI, and amyloid and tau PETs from the ADNI 2/3 database. We evaluated cortical volume, free-water, fractional anisotropy (FA), and amyloid and tau SUVRs in 171 cognitively normal, 103 MCI, and 44 AD individuals. When the 3 groups were combined, increasing amyloid burden was associated with reduced extracellular free-water in the entorhinal cortex and hippocampus in those with amyloid-negative status whereas increasing tau burden was associated with increased extracellular free-water regardless of amyloid status. Next, we found that for the MCI subjects, diffusion measures (free-water, FA) alone predicted MMSE score 2 years later with a high r-square value (87%), as compared to tau SUVRs (27%), T1 volume (36%), and amyloid SUVRs (75%). Diffusion measures represent a potent non-invasive marker for predicting cognitive decline.

Published by Elsevier Inc.

1. Introduction

Alzheimer's disease (AD) is the most common neurodegenerative disease in the elderly population in developed countries (Alzheimer's Association, 2021). It is characterized by extracellular amyloid plaques and intraneuronal neurofibrillary tangles (NFT), formed by tau protein hyperphosphorylation in the brain (Braak & Braak E., 1991; Thal et al., 2002), which lead to irreversible neu-

* Corresponding author at: University of Florida, 1864 Stadium Road, 100 FL-Gym, Gainesville, FL 32611-8205.

E-mail address: vcourt@ufl.edu (D.E. Vaillancourt).

¹ Data used in preparation of this article were obtained from the Alzheimer's Disease Neuroimaging Initiative (ADNI) database (adni.loni.usc.edu). As such, the investigators within the ADNI contributed to the design and implementation of ADNI and/or provided data but did not participate in analysis or writing of this report. A complete listing of ADNI investigators can be found at: http://adni.loni.usc.edu/wp-content/uploads/how_to_apply/ADNI_Acknowledgement_List.pdf.

rologic deterioration and loss of cognitive function. In-vivo neuroimaging biomarkers derived from positron emission tomography (PET) and magnetic resonance imaging (MRI) techniques have been widely used in establishing an AD or mild cognitive impairment (MCI) diagnosis and predicting disease progression (Jack et al., 2010; Tabarestani et al., 2020; Veitch et al., 2019; Bejanin et al., 2017). Although amyloid PET and tau PET imaging have high sensitivity for differentiating AD patients from healthy controls (Maass et al., 2017), the cost of these scans is relatively high due to the complexity of the procedure and necessary instrumentation. For the past 2 decades, diffusion imaging (dMRI) has gained significant traction in detecting tissue integrity in the prodromal stage of AD when volumetric changes are not yet detectable. Specifically, alterations in limbic and commissural white matter tracts were found to be an important biomarker for MCI (Liu et al., 2011; Lo Buono et al., 2020), while changes in diffusion properties in the hippocampus and amygdala are robust findings in differentiating AD from controls (Billeci et al., 2020). However, evidence of dif-

fusion changes in relation to amyloid and tau pathology remains limited, specifically in gray matter where AD pathology primarily occurs (Montal et al., 2018; Vemuri et al., 2017).

Characterizing diffusion measures in gray matter is not trivial. One of the challenges is that tissue voxels are contaminated with cerebrospinal fluid, which alters the signal from the tissue. This challenge is common in AD patients due to a higher degree of brain atrophy (Henf et al., 2018). A novel *d*MRI analysis technique, free-water mapping explicitly estimates extracellular diffusing water from tissue using a 2-compartment model, which offers a more specific measurement of diffusive properties of the brain compared to conventional measures such as FA, which is susceptible to partial volume effects (Pasternak, Sochen, Gur, Intrator, & Assaf, 2009). Increases in free-water is often associated with myelin alterations and neuroinflammation, which can occur during neurodegeneration in AD (; Ofori et al., 2019; Pasternak et al., 2009). The goal of this study was to examine the relationship between amyloid and tau deposition and diffusion changes in gray matter across brain regions categorized by Thal and Braak staging in controls, MCI, and AD. In addition, we utilized support vector machine (SVM) learning regression to predict subjects' cognitive function at baseline and 2 years later based on imaging data.

Due to the nature of high dimensional imaging data from multiple modalities, machine learning offers a powerful approach to predict clinical outcomes Grueso and Viejo-Sobera, 2021. In this study, we further compare the predictive performance of the models using different imaging features. We systematically evaluated the *r*-squared values and root-mean-square error of 4 types of neuroimaging features (structural, amyloid, tau and *d*MRI), both individually and in combination to predict subjects' baseline MMSE score and their MMSE score 2 years later.

2. Materials and methods

2.1. Participants

Imaging data were obtained from the Alzheimer's Neuroimaging Initiative (ADNI) databases Phase 2 and Phase 3 (adni.loni.usc.edu). The primary goal of ADNI is to develop clinical, imaging, genetic, and biochemical biomarkers for the early detection and tracking of AD. For up-to-date information, see www.adni-info.org. This study included subjects with at least 1 T1/*d*MRI scan, 1 amyloid PET scan, and 1 tau PET scan. First, we chose the subjects based on the availability of tau PET and then selected the MRI and amyloid PET acquired closest to the time when the tau PET scan was collected. Subject's diagnosis was determined based on the variable "DIAGNOSIS" from ADNI2 and ADNI3. All subjects recruited were between ages 55–90. To characterize the study participants, the Clinical Dementia Rating scale Sum of Boxes (CDR-SB) score, the number of ApoE ϵ 4 alleles, global amyloid SUVRs (SUMMARYSUVR_WHOLECEREBNORM), and baseline and approximately 2-year follow-up Mini-Mental State Exam (MMSE) scores were used. Baseline MMSE (T_0) scores were retrieved closest to the acquisition day of their T1 MR scans.

2.2. T1 acquisition and analyses

The ADNI T1 scans were acquired with a sagittal 3D Accelerated MPRAGE/IRSPG sequence using a 3T scanner and were collected on the same day as the *d*MRI scans. T1 scan parameters were as follows: repetition time (TR) = 6.96 ms, echo time (TE) = 2.83 ms, flip angle = 11°, slice thickness = 1.2 mm, acquisition matrix = 256×256×196 mm in the *x*-, *y*-, and *z*-dimensions with a voxel size of 1.0×1.0×1.2 mm³.

The T1 scans were processed using FreeSurfer version 7.1.0 (<http://surfer.nmr.mgh.harvard.edu/>). The FreeSurfer package provides automatic preprocessing steps for motion correction, intensity normalization, skull stripping, subcortical segmentation, cortical parcellation, and anatomical labelling (<http://surfer.nmr.mgh.harvard.edu/fswiki/recon-all/>). Volumetric T1 data were obtained with FreeSurfer segmentation for all cortical and subcortical regions using the Desikan-Killiany atlas (Desikan et al., 2006). T1 volumetric data were then divided by subject's estimated total intracranial volume (eTIV) generated by FreeSurfer allowing us to account for the variability of individual head size (Buckner et al., 2004).

2.3. *d*MRI acquisition and analyses

Axial diffusion weighted images were acquired on a 3T scanner with a whole-brain echo planar sequence with the following parameters: diffusion directions = 64, b-value = 1000 s/mm², number of b0 images = 5, TR = 13000 ms, TE = 68.3 ms, in-plane resolution = 2×2 mm, slice thickness = 2.7 mm (no gap), acquisition matrix = 256×256 in-plane, number of slices = 59.

Diffusion MRI scans were processed using image processing tools from the FMRIB Software Library (Smith et al., 2004) and custom UNIX shell scripts. The diffusion MRI processing was consistent with our previous work (Archer et al., 2019b). Eddy corrections using affine transforms were used to correct for head motion and eddy-current distortions (<http://www.fmrib.ox.ac.uk/fsl>). Gradient directions were subsequently rotated to reflect these corrections (Leemans & Jones, 2009). A skull-stripping algorithm was used (BET) to remove non-brain tissue from the image, and a diffusion tensor model was fit at each voxel to determine voxel-wise FA and MD. Free-water maps were calculated using a custom MATLAB script consistent with prior work (Archer et al., 2019a; Ofori et al., 2019; Pasternak et al., 2009). To generate a standardized ROI label corresponding to subjects' T1 anatomical boundaries, individual FA, MD, and free-water images were registered to each subject's corresponding T1 image and segmented mask in native space using a FLIRT affine transformation (Smith et al., 2004). Regional FA, MD, and free-water values for each ROI were extracted based on each subject's cortical parcellation and subcortical segmentation files generated by the FreeSurfer analysis. To harmonize diffusion scans collected from different scanners, we adjusted the diffusion measures using the ComBat batch-effect correction tool (Johnson et al., 2007) as it has shown effectiveness in preserving biological variability and removing unwanted variation introduced by site for diffusion tensor imaging data (Fortin et al., 2017).

2.4. Amyloid/tau PET acquisition and analyses

Amyloid SUVR data were downloaded from the UC Berkeley Florbetapir (AV45) datasets on the ADNI website (<https://adni.loni.usc.edu>). The processing of amyloid PET and the calculation of SUVRs were described in previous work and are also reported on the website (Jagust et al., 2009; Mormino et al., 2009). The regional amyloid SUVR for each ROI was normalized by dividing by the whole cerebellum value (WHOLECEREBELLUM_SUVR). To determine a positive amyloid scan, a cutoff of 1.11 SUVR of the global amyloid level was used (S. M. Landau et al., 2012; S. Landau, Murphy, Lee, Ward, & Jagust, 2021).

Tau SUVR data were downloaded from the UC Berkeley Flortaucipir (AV1451) partial volume-corrected datasets from the ADNI website. The processing of tau PET, calculation of SUVRs and subsequent corrections have been described in previous work and are reported on the website (Baker, Lockhart, et al., 2017; Baker, Maass, et al., 2017). The regional tau SUVR was normalized by dividing

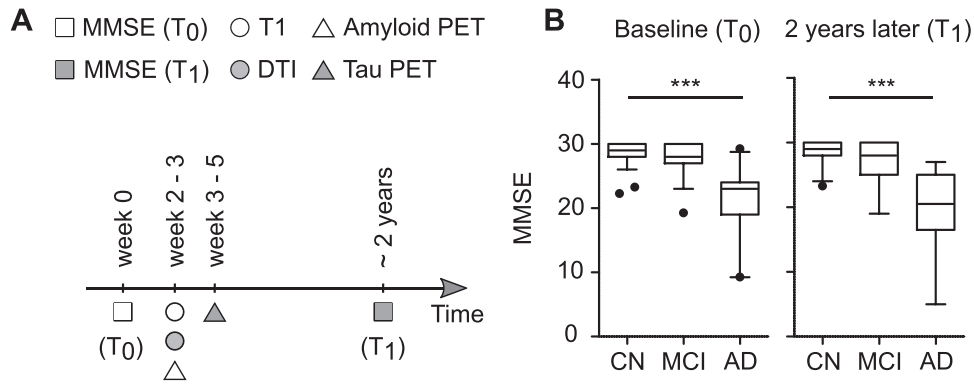


Fig. 1. Timeline of the acquisition of neuroimaging scans and cognitive assessments. (A) Intervals of the T1, diffusion MR (DTI), and amyloid/tau PET scans. Baseline MMSE (T_0) was assessed at week 0. 2–3 weeks after T_0 , structure MRI, diffusion MRI, and amyloid PET scans were collected. A median of a 12-day interval between the collection of MRIs and amyloid PETs was observed. 3–5 weeks after T_0 , tau PETs were collected. Follow-up MMSE scores (T_1) were obtained approximately 2 years after the baseline (mean=821 days, SD=200). Significant differences in the baseline MMSE scores and 2-year follow up MMSE scores were found among the 3 groups *** ($AD < MCI < CN$).

by the inferior cerebellar gray matter reference region value (INFERIOR_CEREBGM_SUVr) (Baker, Lockhart, et al., 2017; Baker, Maass, et al., 2017). Due to the contamination issue with the tau SUVrs in the left and right hippocampus reported by ADNI, we removed the hippocampal tau SUVrs from all our analyses.

2.5. Timeline of imaging acquisition and cognitive measurements

Fig. 1A shows the timeline of the acquisition of neuroimaging modalities and cognitive assessments. Baseline MMSE (T_0) occurred at week 0. Two to 3 weeks after the baseline (T_0), MRI scans (T1 & dMRI) and amyloid PETs were collected. The median interval between the collection of MRI scans and amyloid PETs was 12-days. 3–5 weeks after T_0 , tau PETs were collected. MMSE scores (T_1) were obtained approximately 2 years after the T_0 (mean = 821 days, SD = 200).

2.6. Region of interest analyses

T1 volumetric measures, diffusion measures (free-water, FA, MD), amyloid SUVrs and tau SUVrs for each brain region were originally obtained separately from the left and right hemispheres. To reduce the number of comparisons, we averaged data from the 2 hemispheres of each subject. There are a total of 36 ROIs used for the volumetric and diffusion measures (see the full list of ROIs in Table 2), 43 ROIs for the amyloid SUVrs based on the Thal staging (Supplementary Table 4) (Thal et al., 2002), and 27 ROIs for tau SUVrs based on the Braak staging (Supplementary Table 5). The choice of the ROIs for PET SUVrs were based on the data availability in the ANDI database and previous literature (Braak & Braak E., 1991; Thal et al., 2002). For T1 and diffusion measures, the ROIs were selected based on the segmentation maps generated by FreeSurfer, and based on Braak staging.

2.7. Statistical methods

Demographic and clinical data were compared between the CN, MCI, and AD groups using the Chi-square test for categorical variables and one-way ANOVA for continuous. Non-parametric permutation ANOVA was performed when the assumptions of normality and equal variance were violated. To characterize differences in T1 volumetric data, diffusion measures (free-water, FA, MD), amyloid SUVrs and tau SUVrs among the 3 groups, one-way ANCOVA analyses were conducted for each ROI, with group as the independent variable (CN, MCI, AD), imaging data as the dependent variable,

and age, sex, education, and total number of APOE $\epsilon 4$ alleles as the covariates.

To delineate the relationship between diffusion measures and amyloid and tau deposition for each ROI, partial correlation analyses were conducted using Spearman's non-parametric partial correlation coefficient adjusting for age, sex, education, and total number of APOE $\epsilon 4$ alleles for all 3 groups combined and for each diagnostic group separately. Furthermore, to examine the effect of amyloid status on the relationship of diffusion measures and SUVrs, we split the groups into amyloid-negative and amyloid-positive subgroups. All p -values from the analyses were corrected using false discovery rate (FDR) to control for multiple comparisons based on the number of ROIs (Benjamini & Hochberg, 1995).

To predict subjects' MMSE scores, support vector machine (SVM) regression analyses were performed using different combinations of imaging modalities as input features (MRI volume, free-water, FA, amyloid SUVrs, tau SUVrs). The output variables were either MMSE scores at baseline (T_0) or MMSE scores approximately 2 years later (T_1). Subjects' demographics including age and sex were included as covariates in addition to the imaging modalities across all 15 models. Note that when predicting subjects' MMSE scores 2 years later, age, sex, the follow-up time between baseline and follow-up MMSE was included in each imaging model as covariates. As MCI participants were likely to experience cognitive decline over 2 years, the models were built based on the data from the MCI group only. Radial basis function (RFB) kernel were used. The analyses were performed using the scikit-learn package in Python 3.6. The input features included T1 volumetric measures, diffusion measures (free-water, FA), amyloid SUVrs, and tau SUVrs from the 10 selected ROIs across the 6 Braak stages (Braak I: entorhinal cortex, Braak II: hippocampus (parahippocampal gyrus for tau SUVrs), Braak III: amygdala, lingual gyrus, Braak IV: middle temporal gyrus, temporal pole, Braak V: precuneus, superior frontal gyrus, Braak VI: cuneus gyrus, paracentral gyrus). These ROIs were selected based on the top 2 regions with the highest counts of significant correlations between diffusion measures (free-water, FA) and amyloid SUVrs and tau SUVrs for each Braak stage before FDR correction. In addition, a predictive model using subject's demographic data only (sex, age) as input features were built as a reference model. Data were randomly split into a training and validation dataset, which consisted of 80% of total data, and a test dataset, which consisted of 20% of the remaining data. To ensure that the group proportions in the training and validation and test dataset was similar to the group proportions in the entire data, stratified sampling based on subject's diagnosis was applied. Data normalization was then performed. Specifically,

Table 1
Demographics and clinical data.

	CN (n = 171)	MCI (n = 103)	AD (n = 44)	Statistics	Post-hoc comparison
Age	74.2 ± 7.0	75.6 ± 7.2	77.1 ± 7.9	$F = 3.3, p = 0.04$	A-C
Sex (M/F)	63/108	62/41	25/19	$\chi^2 = 16.0, p < 0.01$	
Education (y)	16.4 ± 2.5	16.7 ± 2.7	15.7 ± 2.4	$p = 0.09$	
CDR-SB score	0.16 ± 0.4	1.4 ± 1.2	5.57 ± 3.64	$p < 0.01$	M-C / A-C / A-M
Number of APOE $\epsilon 4$ alleles				$\chi^2 = 19.0, p < 0.01$	
0	110	61	20		
1	52	23	16		
2	4	15	6		
NA	5	4	2		
Global amyloid SUVRs	1.14 ± 0.2	1.23 ± 0.3	1.37 ± 0.2	$p < 0.01$	M-C / A-C / A-M
Amyloid positivity (-/+)	102/69	50/53	7/37	$\chi^2 = 27.0, p < 0.01$	
Baseline MMSE (T_0)	29.0 ± 1.3	27.9 ± 2.1	21.2 ± 5.2	$p < 0.01$	M-C / A-C / A-M
MMSE 2 y after (T_1) ^a	28.9 ± 1.4	26.8 ± 3.3	20.0 ± 6.2	$p < 0.01$	M-C / A-C / A-M

Data are either count or mean ± SD.

Key: CN, control; MCI, mild cognitive impairment; AD, Alzheimer's disease; CDR-SB, Clinical Dementia Rating scale Sum of Boxes; MMSE, Mini-Mental State Examination. Key: A-C, significant difference between AD and CN; A-M, significant difference between AD and MCI; M-C, significant difference between MCI and CN.

^a Data from the 2-year follow up (105 controls, 58 MCI, and 12 AD).

the mean and the variance of the training and validation dataset were used to normalize the training and validation dataset, and the test dataset. Based on the training and validation dataset, for each model, hyperparameters were tuned using a 5-fold cross validation grid search for optimal prediction. Predictive performance (r-squared) from the SVM regression was then evaluated on the test dataset for each model.

3. Results

3.1. Demographics and clinical data

Data used in this study were from 171 CN (mean age; 74.2 ± 7.0), 103 MCI (mean age; 75.6 ± 7.2), and 44 AD (mean age; 77.1 ± 7.9) subjects who had at least 1 scan for all 4 imaging modalities, i.e. T1, dMRI, amyloid PET, and tau PET (Table 1, Fig. 1A). The AD subjects were slightly older than the controls ($p = 0.04$). No differences were found in education ($p = 0.09$). A significant difference between the 3 groups was found in sex ($p < 0.01$), CDR-SB ($p < 0.01$), number of APOE $\epsilon 4$ alleles ($p < 0.01$), global amyloid SUVRs ($p < 0.01$), and amyloid positivity count ($p < 0.01$). There were more females in the CN group and more males in the MCI and AD groups. Significant group differences in the MMSE scores both at baseline (T_0 , $p < 0.01$) and at the 2-year follow up (T_1 , $p < 0.01$) were found. The post-hoc analyses showed that significant differences in MMSE among the 3 groups (AD < MCI < CN) (multiple p values from post-hoc, $ps < 0.01$).

3.2. Regional cortical volume, diffusion measures, regional amyloid SUVRs, and tau SUVRs

The mean cortical volume, diffusion measures (FW, FA, and MD), amyloid SUVRs, and tau SUVRs were computed for regional gray matter ROIs in the CN, MCI, and the AD group. Fig. 2 shows the between-group results from 10 selected gray matter ROIs across Braak stages/ Thal phases for each imaging measure; note that bar graphs from top to bottom represent the same ROI. (MRI volume: Fig. 2A, Supplementary Table 1; free-water: Fig. 2B, Table 2; FA: Fig. 2C, Supplementary Table 2; MD: Supplementary Table 3; Amyloid: Fig. 2E, Supplementary Table 7; Tau: Fig. 2D, Supplementary Table 8). After adjusting for age, sex, education, and total number of APOE $\epsilon 4$ alleles, significant main effects of group on cortical volume and diffusion measures were found among all 3 groups in widespread ROIs across Braak stages I–VI, with significant cortical atrophy, higher free-water values/MD, and lower

FA for the AD group. For regional amyloid SUVRs, significant differences among all 3 groups (AD > MCI > CN) were found in all the neocortex ROIs in the Phase 1 Thal stage and in numerous limbic, subcortical, and brain stem ROIs in Phase 2–4 Thal stages. While a general pattern of increasing amyloid SUVRs from CN to AD subjects was shown across multiple ROIs, amyloid SUVR in the hippocampus was found to be significantly lower in the AD group compared to the MCI and CN groups. For regional tau SUVRs, significant differences among all 3 groups (AD > MCI > CN) in numerous gray matter ROIs across Braak stages were found. To examine the effect of different types of scanners on the diffusion data, Supplementary Tables 4–6 show the between-group result using adjusted diffusion measures for free-water, FA, and MD. Changes in significance before and after applying the harmonization tool are marked by gray shading. Overall, the effect was minimal, although FA measures were more susceptible to different scanners.

3.3. Partial correlation analyses between diffusion measures and amyloid/tau SUVRs

We performed partial correlation analyses between free-water values and amyloid SUVRs (Table 3), and between free-water values and tau SUVRs across ROIs (Table 4) for all 3 groups combined, and for each diagnostic group separately. The p -values from the subgroup analysis split by amyloid positivity were also reported (a-: amyloid negative; a+: amyloid positive). In Table 3, when all 3 groups were combined, we observed significant negative correlations across multiple ROIs in the amyloid-negative subgroup. Furthermore, for the MCI group, we found significant correlations in the entorhinal cortex ($r_{\text{part}} = -0.52, p_{\text{adj}} < 0.01$) and hippocampus ($r_{\text{part}} = -0.56, p_{\text{adj}} < 0.01$) in those who had amyloid negative status (Figs. 3C and 3D). No correlations were found in the amyloid positive subgroup in the MCI group nor in the AD group (Figs. 3E and 3F).

For tau SUVRs (Table 4), when all 3 groups combined, significant positive correlations were found across multiple ROIs across Braak stages. The significance in multiple ROIs continued to be observed in both amyloid-negative and amyloid-positive subgroups. For each diagnosis group, significant correlations between free-water and tau SUVRs were found in the MCI group and AD group in the ROIs in the early Braak stages, including entorhinal cortex (Fig. 4A), amygdala, and parahippocampus (Fig. 4B). For the entorhinal cortex, significant positive correlations continued to be shown in the amyloid-positive subgroup in the MCI group ($r_{\text{part}} = 0.40, p_{\text{adj}} = 0.04$), and the AD groups ($r_{\text{part}} = 0.46, p = 0.01$)

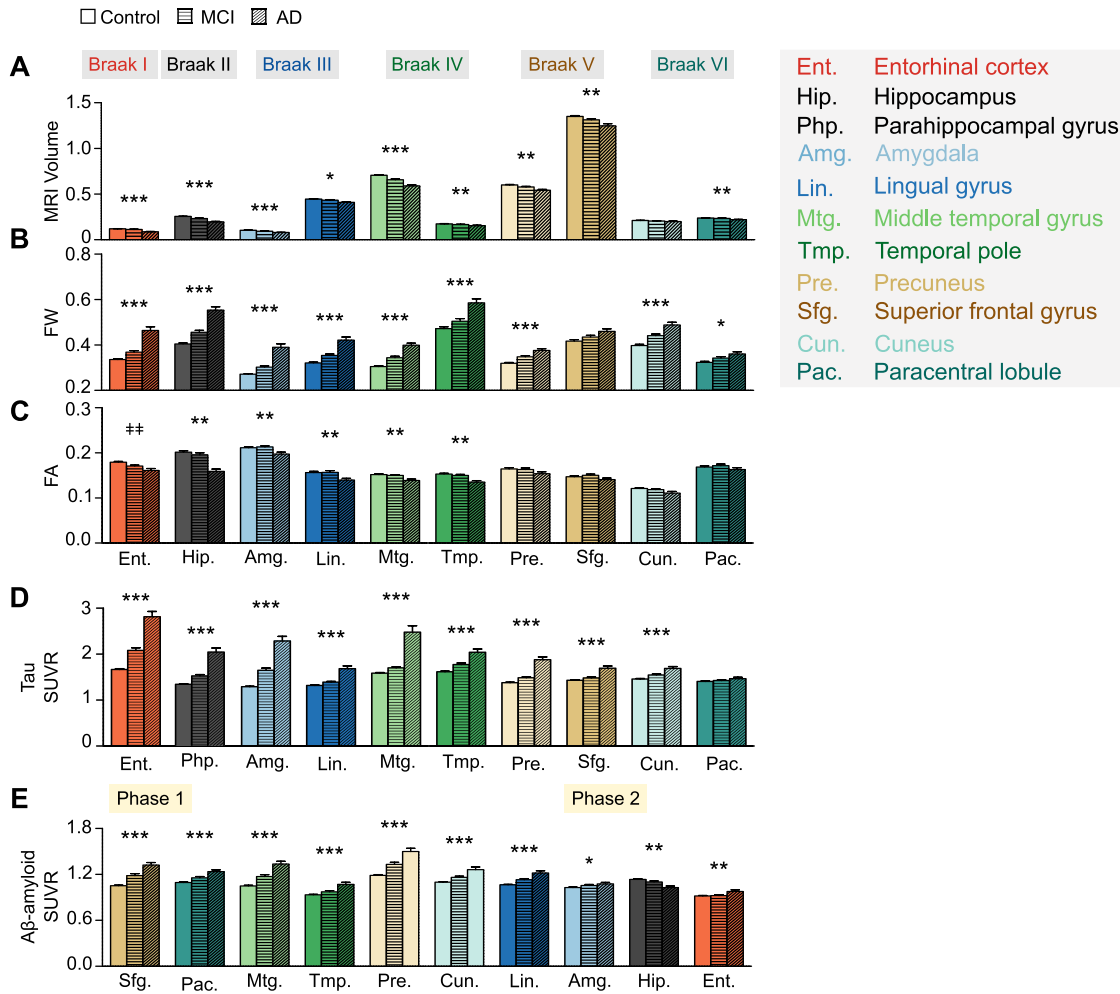


Fig. 2. Mean cortical volume, diffusion measures (free-water & FA), and regional SUVRs (amyloid & tau) in the selected ROIs in the control, MCI, and AD groups. The ROIs in the (A–D) are in the order of Braak stages while the amyloid ROIs are in the order of Thal phases. Due to the contamination issue with tau SUVR in the hippocampal region, tau SUVRs in the parahippocampal gyrus was shown instead. *** Significant differences between the AD vs. CN, MCI vs. CN, and MCI vs. AD. ** Significant differences between the AD vs. CN, and MCI vs. AD. †† Significant differences between the AD vs. CN, and MCI vs. CN. * Significant difference between the AD vs. CN.

before FDR correction, $p_{adj} = 0.07$ (Fig. 4E). For the parahippocampus, a significant positive correlation was found in the amyloid-positive subgroup in the AD group ($r_{part} = 0.56$, $p_{adj} = 0.02$, Fig. 4F).

For the FA measure, the direction between free-water and amyloid SUVRs was reversed (Supplementary Table 9). We observed significant positive correlations between FA and amyloid SUVRs in the hippocampus when all 3 groups were combined ($r_{part} = 0.31$, $p_{adj} < 0.01$) and in the MCI group ($r_{part} = 0.32$, $p_{adj} = 0.03$).

For the relationship between FA and tau SUVRs (Supplementary Table 11), significant negative correlations in all 3 groups combined were found in multiple ROIs across Braak stages, including entorhinal cortex ($r_{part} = -0.27$, $p_{adj} < 0.01$) and parahippocampus ($r_{part} = -0.19$, $p_{adj} < 0.01$). In addition, when splitting the group based on amyloid status, significant negative correlations remained in the entorhinal cortex and parahippocampus for both subgroups.

For the MD measure, when all 3 groups were combined, we observed significant negative correlations between MD and amyloid SUVRs in only those with amyloid-negative status (Supplementary Table 10). For the relationship between MD and tau SUVRs, when all 3 groups were combined, significant positive correlations were found in multiple ROIs and also in those with amyloid-positive status (Supplementary Table 12).

3.4. Prediction of MMSE using different imaging modalities

Fig. 5 shows the r-squared values and the root-mean-square error (RMSE) of the SVM regression models using different combinations of imaging modalities with age and sex to predict subjects' MMSE score at baseline (T_0) and 2 years later (T_1) in the MCI group. When predicting follow-up MMSE scores (Fig. 5C–5D), age, sex, and follow-up time in addition to imaging modalities were included across all 15 models. There are 103 MCI subjects included in the prediction of the baseline MMSE scores (T_0) and 58 MCI subjects included in the prediction of the 2-year follow-up MMSE scores (T_1). When predicting the baseline MMSE, diffusion measures alone (free-water & FA, $R^2_{DTI} = 96\%$, $RMSE_{DTI} = 0.15$, model 3, Fig. 5A–5B), and combining MRI volume and diffusion measures achieved the highest r-square value ($R^2_{MRI\ volume+DTI} = 96\%$, $RMSE_{MRI\ volume+DTI} = 0.13$, model 10). MRI volume alone explained the lowest proportion of variance in the baseline MMSE scores ($R^2_{MRI\ volume} = 4\%$, $RMSE_{MRI\ volume} = 0.69$, Model 2).

When predicting MMSE scores 2 years later (T_1), combining tau PET and diffusion measures achieved the highest r-square ($R^2_{\tau+DTI} = 97\%$, $RMSE_{\tau+DTI} = 0.19$, Model 9, Fig. 5C–5D). Diffusion measures alone explained the second highest proportion of variance ($R^2_{DTI} = 87\%$, $RMSE_{DTI} = 0.37$, Model 3). When comparing

Table 2

Mean free-water values in 36 gray matter regions for the CN, MCI, and the AD group, and the statistical results from the ANCOVA analyses in comparing between the 3 groups. Abbreviations: A–C, significant difference between AD and CN, A–M, significant difference between AD and MCI, M–C, significant difference between MCI and CN.

ROIs	CN		MCI		AD		Corrected <i>p</i> -value	Post-hoc comparison
	Mean	SE	Mean	SE	Mean	SE		
Braak I								
Entorhinal cortex	0.336	0.004	0.368	0.007	0.464	0.016	< 0.01	M–C / A–C / A–M
Braak II								
Hippocampus	0.404	0.004	0.456	0.008	0.553	0.015	< 0.01	M–C / A–C / A–M
Braak III								
Amygdala	0.271	0.002	0.302	0.005	0.390	0.015	< 0.01	M–C / A–C / A–M
Lingual gyrus	0.321	0.003	0.354	0.006	0.421	0.013	< 0.01	M–C / A–C / A–M
Parahippocampal gyrus	0.310	0.003	0.337	0.005	0.408	0.011	< 0.01	M–C / A–C / A–M
Fusiform gyrus	0.245	0.002	0.276	0.004	0.341	0.010	< 0.01	M–C / A–C / A–M
Braak IV								
Middle temporal gyrus	0.305	0.004	0.344	0.006	0.399	0.009	< 0.01	M–C / A–C / A–M
Temporal pole	0.472	0.008	0.504	0.012	0.585	0.018	< 0.01	M–C / A–C / A–M
Caudal anterior cingulate	0.376	0.005	0.412	0.007	0.458	0.013	< 0.01	M–C / A–C / A–M
Rostral anterior cingulate cortex	0.359	0.004	0.387	0.005	0.428	0.010	< 0.01	M–C / A–C / A–M
Posterior cingulate cortex	0.358	0.006	0.396	0.008	0.441	0.013	< 0.01	M–C / A–C / A–M
Isthmus of cingulate gyrus	0.275	0.003	0.304	0.005	0.365	0.011	< 0.01	M–C / A–C / A–M
Insula	0.298	0.004	0.325	0.006	0.370	0.010	< 0.01	M–C / A–C / A–M
Inferior temporal gyrus	0.235	0.002	0.266	0.005	0.315	0.009	< 0.01	M–C / A–C / A–M
Braak V								
Precuneus	0.319	0.004	0.348	0.005	0.376	0.008	< 0.01	M–C / A–C / A–M
Superior frontal gyrus	0.417	0.006	0.435	0.007	0.460	0.011	0.03	
Lateral orbitofrontal cortex	0.248	0.002	0.275	0.004	0.293	0.006	< 0.01	M–C / A–C / A–M
Medial orbitofrontal cortex	0.340	0.004	0.371	0.005	0.405	0.007	< 0.01	M–C / A–C / A–M
Frontal pole	0.341	0.007	0.391	0.011	0.432	0.022	< 0.01	M–C / A–C / A–M
Caudal middle frontal	0.404	0.007	0.430	0.008	0.471	0.015	< 0.01	A–C
Rostral middle frontal gyrus	0.389	0.006	0.422	0.007	0.457	0.014	< 0.01	M–C / A–C
Pars opercularis	0.327	0.004	0.357	0.005	0.413	0.012	< 0.01	M–C / A–C / A–M
Pars orbitalis	0.283	0.003	0.316	0.006	0.343	0.010	< 0.01	M–C / A–C
Pars triangularis	0.321	0.004	0.362	0.007	0.403	0.011	< 0.01	M–C / A–C / A–M
Lateral occipital gyrus	0.267	0.003	0.308	0.005	0.378	0.012	< 0.01	M–C / A–C / A–M
Supramarginal gyrus	0.337	0.004	0.372	0.005	0.410	0.010	< 0.01	M–C / A–C / A–M
Inferior parietal lobule	0.323	0.005	0.355	0.006	0.403	0.009	< 0.01	M–C / A–C / A–M
Superior temporal gyrus	0.412	0.005	0.437	0.006	0.498	0.011	< 0.01	A–C / A–M
Superior parietal lobule	0.385	0.007	0.425	0.009	0.450	0.014	< 0.01	M–C / A–C
Superior temporal sulcus	0.242	0.003	0.275	0.005	0.331	0.009	< 0.01	M–C / A–C / A–M
Transverse temporal gyrus	0.548	0.007	0.577	0.009	0.651	0.016	< 0.01	A–C / A–M
Braak VI								
Cuneus	0.397	0.006	0.441	0.007	0.488	0.012	< 0.01	M–C / A–C / A–M
Paracentral gyrus	0.323	0.004	0.342	0.006	0.360	0.010	< 0.01	A–C
Pericalcarine cortex	0.306	0.004	0.331	0.006	0.395	0.013	< 0.01	M–C / A–C / A–M
Postcentral gyrus	0.407	0.005	0.434	0.007	0.466	0.011	< 0.01	M–C / A–C
Precentral gyrus	0.385	0.006	0.410	0.008	0.443	0.013	< 0.01	A–C

each individual modality (model 1–4), diffusion measure only showed the highest r-square in predicting both baseline MMSE and the 2-year follow-up. In addition, we built a model based on subject's demographic data only (age, sex). For predicting baseline MMSE, the demographic model showed 7% r-squared values. For predicting follow-up MMSE, age, sex, baseline MMSE, and follow-up time were able to achieve 89% r-square value.

4. Discussion

We report 3 key findings. First, significant increases in free-water and decreases in FA were evident in gray matter in multiple brain regions across Braak stages in the MCI and AD groups compared to the CN group. Second, when the 3 groups were combined, significant negative correlations were found between free-water and amyloid SUVrs in those with amyloid negative status, while positive correlations were found between free-water and tau SUVrs regardless of amyloid status. Third, diffusion measures alone from the selected gray matter ROIs revealed high r-squared values in predicting MCI subjects' MMSE scores at baseline (96% R^2) and 2 years later (87% R^2). Our findings revealed associations between microstructural changes in gray matter, extracellular amyloid plaques, and intracellular tau proteins, providing insights

into the possible underlying cellular processes associated with AD pathology. Diffusion changes in gray matter regions provide valuable information for predicting cognitive decline after 2 years in MCI subjects.

The significantly elevated free-water and reduced FA in the MCI and AD groups map to the established anatomical regions of the histopathological staging of AD. The result extends and confirms previous dMRI studies, which consistently showed aberrant diffusion changes, such as FA and MD in these regions in MCI and AD (Choo et al., 2010; Jacobs et al., 2013; Lee et al., 2020; Scola et al., 2010; Weston et al., 2015). We have now extended these findings to free-water measures and characterization of amyloid and tau accumulation derived from the same gray matter regions in a larger cohort. We used the automated segmentation provided by FreeSurfer to eliminate partial volume effects and generate more accurate ROIs (Henf et al., 2018). We found a greater number of significant differences in free-water among all 3 groups in the ROIs across all Braak stages, while between-group differences in FA (AD vs. CN & AD vs. MCI) were observed more consistently in the early Braak stages. Free-water estimates the volume of the extracellular space, and increases in free-water can occur during neuroinflammation (Pasternak et al., 2018a), which is often associated with the neurodegenerative processes in AD. Loss of neuron

Table 3
 Partial correlation analyses of free-water values with regional amyloid SUVRs in 43 gray matter ROIs for all 3 groups combined (All), and individual groups (CN, MCI, and AD). *p*-values resulted from the subgroup-analysis based on the amyloid positivity are reported (a-:amyloid negative; a+:amyloid positive) **p*_{adj} < 0.05 after FDR correction. *r*_{part}: Spearman's partial correlation coefficient adjusting for age, gender, education, and total number of APOE alleles.

ROIs	FW															
	Amyloid SUVR															
	All				CN				MCI				AD			
R	<i>p</i>	<i>p</i> (a-)	<i>p</i> (a+)	<i>r</i>	<i>p</i>	<i>p</i> (a-)	<i>p</i> (a+)	<i>r</i>	<i>p</i>	<i>p</i> (a-)	<i>p</i> (a+)	<i>r</i>	<i>p</i>	<i>p</i> (a-)	<i>p</i> (a+)	
Phase 1																
Frontal lobe																
Superior frontal gyrus	-0.12	0.21	< 0.01	0.64	-0.17	0.12	0.11	0.93	-0.22	0.42	0.81	0.93	-0.29	0.25	0.71	0.28
Lateral orbitofrontal cortex	0.00	0.99	0.03	0.32	-0.11	0.30	0.21	0.86	-0.14	0.61	0.81	0.64	-0.26	0.29	0.91	0.36
Medial orbitofrontal cortex	0.04	0.77	0.03	0.07	-0.10	0.30	0.15	0.47	-0.06	0.87	0.81	0.87	-0.35	0.18	0.71	0.28
Frontal pole	0.01	0.91	0.53	0.10	-0.08	0.49	0.58	0.66	-0.07	0.84	0.98	0.87	0.26	0.29	0.91	0.28
Caudal middle frontal	-0.03	0.77	< 0.01	0.16	-0.12	0.25	0.06	0.80	-0.12	0.61	0.81	0.64	-0.17	0.52	0.91	0.28
Rostral middle frontal gyrus	-0.02	0.87	0.41	0.06	-0.19	0.09	0.93	0.80	-0.13	0.61	0.81	0.89	0.06	0.75	0.96	0.89
Pars opercularis	0.03	0.77	0.01	0.10	-0.20	0.09	0.04	0.86	0.04	0.89	0.98	0.93	-0.08	0.68	0.91	0.67
Pars orbitalis	-0.04	0.77	0.02	0.10	-0.17	0.12	0.16	0.93	-0.22	0.42	0.84	0.64	0.03	0.87	0.91	0.67
Pars triangularis	0.04	0.77	0.31	0.10	-0.12	0.25	0.61	0.93	-0.07	0.84	0.86	0.89	-0.11	0.61	0.91	0.67
Paracentral gyrus	-0.08	0.50	0.11	0.38	-0.15	0.17	0.12	0.33	-0.10	0.68	0.81	0.89	-0.36	0.18	0.91	0.28
Precentral gyrus	-0.09	0.43	< 0.01	0.73	-0.18	0.09	0.02	0.97	-0.12	0.61	0.81	0.89	-0.24	0.35	0.91	0.28
Temporal lobe																
Superior temporal gyrus	-0.02	0.81	0.70	0.73	-0.19	0.09	0.93	0.16	-0.11	0.64	0.81	0.87	-0.27	0.29	0.91	0.28
Superior temporal sulcus	0.12	0.19	0.17	0.13	-0.02	0.85	0.61	0.93	0.00	1.00	0.99	0.64	-0.29	0.25	0.91	0.32
Middle temporal gyrus	0.07	0.55	0.17	0.06	-0.13	0.22	0.93	0.60	-0.03	0.89	0.81	0.89	-0.41	0.17	0.91	0.28
Inferior temporal gyrus	0.11	0.27	0.13	0.06	-0.15	0.17	0.61	0.40	0.03	0.89	0.98	0.87	-0.28	0.25	0.99	0.33
Fusiform gyrus	0.17	0.04	0.18	0.06	-0.03	0.80	0.28	0.68	0.05	0.87	0.98	0.87	-0.06	0.75	0.91	0.86
Temporal pole	0.01	0.94	0.43	0.51	-0.07	0.55	0.93	0.93	-0.03	0.89	0.81	0.89	-0.33	0.21	0.91	0.32
Transverse temporal gyrus	-0.03	0.81	0.47	0.73	-0.06	0.62	0.94	0.66	-0.13	0.61	0.99	0.64	-0.19	0.47	0.91	0.62
Parietal lobe																
Precuneus	0.07	0.55	< 0.01	0.23	-0.07	0.50	0.02	0.33	0.03	0.89	0.81	0.87	-0.29	0.25	0.91	0.32
Supramarginal gyrus	0.03	0.77	0.17	0.65	-0.13	0.22	0.36	0.16	-0.02	0.90	0.86	0.91	-0.14	0.54	0.91	0.49
Superior parietal lobule	-0.08	0.50	< 0.01	0.54	-0.20	0.09	0.02	0.02	-0.14	0.61	0.81	0.66	-0.22	0.41	0.91	0.28
Inferior parietal lobule	0.06	0.55	0.04	0.75	-0.07	0.50	0.28	0.22	-0.03	0.89	0.81	0.89	-0.18	0.50	0.91	0.33
Postcentral gyrus	-0.08	0.50	0.01	0.73	-0.17	0.12	0.06	0.26	-0.11	0.63	0.81	0.91	-0.34	0.20	0.91	0.28
Occipital lobe																
Cuneus	-0.08	0.50	< 0.01	0.54	-0.23	0.06	0.02	0.33	-0.14	0.61	0.51	0.91	-0.14	0.54	0.91	0.69
Lingual gyrus	0.02	0.87	0.03	0.32	-0.14	0.21	0.07	0.93	-0.04	0.89	0.81	0.87	-0.10	0.64	0.91	0.66
Pericalcarine cortex	-0.05	0.74	0.01	0.55	-0.27	0.02	0.02	0.30	0.00	1.00	0.84	0.89	-0.15	0.54	0.91	0.58
Lateral occipital gyrus	0.14	0.10	0.83	0.07	-0.01	0.95	0.93	0.93	0.00	1.00	0.98	0.77	-0.10	0.65	0.91	0.86
Phase 2																
Entorhinal cortex	-0.05	0.74	0.03	0.70	-0.02	0.85	0.95	0.93	-0.10	0.68	< 0.01	0.87	-0.39	0.17	0.91	0.28
Hippocampus	-0.36	< 0.01	< 0.01	< 0.01	-0.15	0.17	0.28	0.30	-0.44	< 0.01	< 0.01	0.11	-0.38	0.17	0.91	0.28
Insula	0.00	0.96	0.45	0.32	-0.13	0.23	0.93	0.84	-0.12	0.61	0.98	0.64	-0.08	0.68	0.97	0.89
Amygdala	0.01	0.94	0.41	0.45	0.00	0.98	0.61	0.35	-0.13	0.61	0.81	0.64	-0.16	0.54	0.91	0.49
Parahippocampal gyrus	0.06	0.60	0.22	0.73	-0.03	0.80	0.93	0.33	-0.04	0.89	0.98	0.89	-0.23	0.35	0.91	0.45
Caudal anterior cingulate	-0.03	0.81	< 0.01	0.38	-0.12	0.24	0.02	0.35	-0.18	0.61	0.81	0.87	-0.12	0.58	0.91	0.42
Rostral anterior cingulate cortex	-0.02	0.81	< 0.01	0.12	-0.21	0.08	0.06	0.93	-0.05	0.87	0.81	0.93	-0.14	0.54	0.91	0.65
Posterior cingulate cortex	-0.04	0.77	< 0.01	0.73	-0.12	0.25	0.03	0.80	-0.15	0.61	0.81	0.87	-0.45	0.14	0.71	0.21
Isthmus of cingulate gyrus	0.15	0.09	0.07	< 0.01	-0.03	0.80	0.44	0.33	0.08	0.82	0.81	0.89	-0.17	0.52	0.71	0.54
Phase 3																
Thalamus_Proper	-0.07	0.55	0.45	0.32	-0.04	0.80	0.61	0.26	-0.06	0.84	0.84	0.91	-0.31	0.25	0.91	0.33
Caudate	-0.12	0.19	0.02	0.19	-0.13	0.22	0.61	0.25	-0.16	0.61	0.81	0.93	-0.21	0.42	0.91	0.33
Putamen	0.03	0.81	0.54	0.73	0.05	0.66	0.19	0.80	-0.12	0.61	0.84	0.64	-0.15	0.54	0.91	0.28
Pallidum	-0.03	0.77	0.45	0.38	0.02	0.83	0.51	0.93	-0.02	0.92	0.81	0.89	-0.10	0.64	0.91	0.89
Accumbens area	0.10	0.27	0.24	0.10	-0.10	0.30	0.86	0.93	0.18	0.61	0.98	0.87	-0.19	0.47	0.91	0.44
Phase 4																
Brain stem	-0.11	0.22	0.60	0.02	-0.03	0.83	0.61	0.40	-0.07	0.84	0.81	0.64	0.05	0.75	0.91	0.86
Cerebellum Cortex	0.16	0.07	0.21	0.19	0.10	0.30	0.86	0.26	0.17	0.61	0.81	0.87	-0.14	0.54	0.91	0.38

Table 4
 Partial correlation analyses of free-water values with regional tau SUVRs in 28 gray matter ROIs for all 3 groups combined (All), and individual groups (CN, MCI, and AD). P-values resulted from the subgroup-analysis based on the amyloid positivity are reported (a-:amyloid negative; a+:amyloid positive) * $p_{adj} < .05$ after FDR correction. r_{part} : Spearman's partial correlation coefficient adjusting for age, gender, education, and total number of APOE alleles.

ROIs	FW															
	Tau SUVR															
	All				CN				MCI				AD			
	r	p	p (a-)	p(a+)	r	p	p (a-)	p(a+)	r	p	p (a-)	p(a+)	r	p	p (a-)	p(a+)
Braak I																
Entorhinal cortex	0.39	< 0.01	< 0.01	< 0.01	0.06	0.60	0.23	0.95	0.38	< 0.01	0.34	0.04	0.46	0.03	0.41	0.07
Braak II																
Hippocampus	0.33	< 0.01	< 0.01	< 0.01	0.11	0.36	0.23	0.95	0.14	0.25	0.34	0.98	0.32	0.22	0.63	0.81
Braak III																
Amygdala	0.44	< 0.01	0.01	< 0.01	-0.01	0.92	0.86	0.95	0.42	< 0.01	0.01	0.04	0.44	0.03	0.41	0.04
Lingual gyrus	0.26	< 0.01	0.10	< 0.01	-0.01	0.91	0.85	0.98	0.28	0.02	0.25	0.46	0.02	0.96	0.41	0.74
Parahippocampal gyrus	0.43	< 0.01	0.00	< 0.01	0.11	0.36	0.15	0.94	0.29	0.02	0.02	0.32	0.45	0.03	0.83	0.02
Fusiform gyrus	0.47	< 0.01	0.00	< 0.01	0.21	0.07	0.21	0.71	0.27	0.02	0.25	0.33	0.14	0.75	0.83	0.44
Braak IV																
Middle temporal gyrus	0.31	< 0.01	0.23	< 0.01	-0.02	0.87	0.73	0.88	0.24	0.04	0.84	0.04	0.12	0.75	0.67	0.36
Temporal pole	0.12	0.04	0.91	0.04	-0.16	0.12	0.32	0.71	0.22	0.06	0.34	0.57	0.35	0.16	0.67	0.09
Caudal anterior cingulate	0.02	0.75	0.19	0.17	-0.08	0.47	0.32	0.98	0.06	0.61	0.77	0.50	0.00	1.00	0.73	0.81
Rostral anterior cingulate cortex	0.09	0.12	0.83	0.23	-0.03	0.83	0.85	0.71	0.15	0.22	0.84	0.28	0.15	0.75	0.83	0.50
Posterior cingulate cortex	0.22	< 0.01	0.24	< 0.01	-0.01	0.91	0.85	0.95	0.25	0.03	0.67	0.06	-0.12	0.75	0.41	0.98
Isthmus of cingulate gyrus	0.25	< 0.01	0.55	< 0.01	-0.08	0.50	0.91	0.71	0.08	0.52	0.84	0.92	0.21	0.75	0.41	0.35
Insula	0.21	< 0.01	0.23	< 0.01	-0.04	0.73	0.73	0.95	0.17	0.16	0.34	0.46	0.17	0.75	0.92	0.68
Inferior temporal gyrus	0.40	< 0.01	0.01	< 0.01	0.09	0.46	0.30	0.98	0.27	0.02	0.36	0.07	-0.07	0.96	0.43	0.96
Braak V																
Precuneus gyrus	0.34	< 0.01	0.01	< 0.01	0.06	0.60	0.69	0.97	0.29	0.02	0.34	0.10	0.02	0.96	0.79	0.74
Superior frontal gyrus	-0.07	0.22	0.05	0.96	-0.23	0.07	0.25	0.30	-0.03	0.73	0.34	0.46	-0.02	0.96	0.73	0.90
Lateral orbitofrontal cortex	0.34	< 0.01	< 0.01	< 0.01	0.19	0.07	0.15	0.95	0.16	0.18	0.34	0.57	-0.09	0.90	0.73	1.00
Supramarginal gyrus	0.21	< 0.01	0.39	< 0.01	-0.01	0.91	0.73	0.95	0.06	0.61	0.89	0.57	0.12	0.75	0.61	0.90
Inferior parietal lobule	0.32	< 0.01	0.04	< 0.01	0.11	0.36	0.48	0.71	0.17	0.18	0.36	0.92	0.16	0.75	0.92	0.74
Superior temporal gyrus	0.17	< 0.01	0.83	< 0.01	-0.06	0.60	0.81	0.95	0.10	0.41	0.70	0.50	0.20	0.75	0.83	0.48
Superior parietal lobule	0.06	0.35	0.79	0.44	-0.09	0.46	0.86	0.46	-0.06	0.61	0.62	0.98	0.05	0.96	0.92	0.98
Superior temporal sulcus	0.38	< 0.01	0.01	< 0.01	0.09	0.46	0.34	0.97	0.27	0.02	0.40	0.06	0.13	0.75	0.58	0.74
Transverse temporal gyrus	0.16	0.01	0.13	0.13	0.19	0.07	0.23	0.85	0.08	0.51	0.73	0.98	-0.14	0.75	0.61	0.95
Braak VI																
Cuneus	0.29	< 0.01	0.01	< 0.01	0.19	0.07	0.23	0.35	0.22	0.06	0.70	0.28	-0.04	0.96	0.58	0.98
Paracentral gyrus	0.00	1.00	0.79	0.67	-0.11	0.37	0.65	0.71	0.12	0.37	0.62	0.58	-0.01	0.96	0.41	1.00
Pericalcarine cortex	0.25	< 0.01	0.01	< 0.01	0.17	0.11	0.65	0.14	0.31	0.01	0.05	0.46	-0.02	0.96	0.58	0.98
Postcentral gyrus	-0.05	0.38	0.69	0.53	-0.15	0.14	0.50	0.46	-0.04	0.71	0.67	0.98	-0.16	0.75	0.79	0.90
Precentral gyrus	-0.09	0.12	0.44	0.44	-0.20	0.07	0.65	0.30	-0.10	0.41	0.34	0.98	-0.03	0.96	0.61	0.98

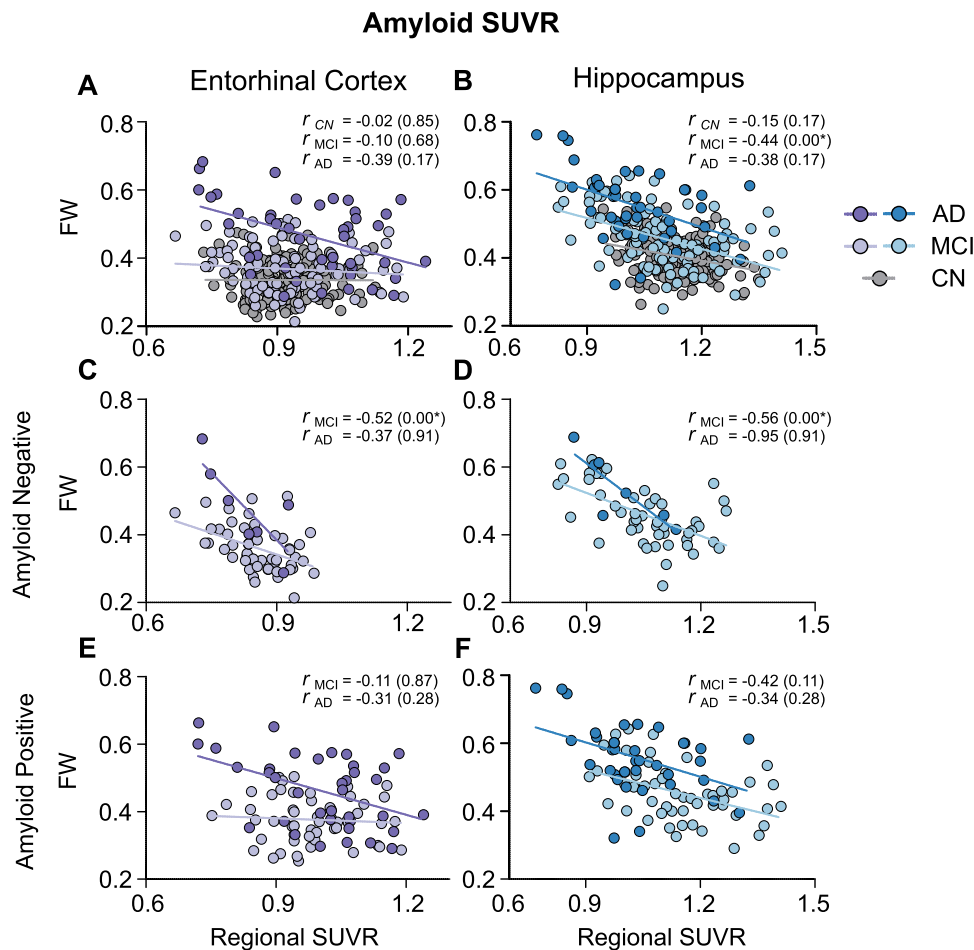


Fig. 3. Partial correlation analyses of free-water values with regional amyloid SUVRs in the entorhinal cortex (**A,C,E**) and the hippocampus (**B,D,F**) for the CN, MCI, and the AD group. Figure **C** and **D** (second row) highlight the data from the MCI and the AD subjects who had amyloid-negative status. Figure **D** and **F** highlight the data from the MCI and the AD who had amyloid-positive status. * $p < 0.05$ after FDR correction.

cell bodies, synapses, and dendrites can also contribute to an increase in extracellular space free-water. Reductions in FA in MCI and AD in white matter, e.g., fornix, corpus callosum and cingulum fibers (Chao et al., 2013; Choo et al., 2010; Pievani et al., 2010; Scola et al., 2010), have been shown. However, interpreting FA results can be challenging because the changes in FA can result from changes of diffusion either parallel or perpendicular to the principle direction of the tensor (Pievani et al., 2010). Characterizing diffusion changes in gray matter is important because pathology in gray matter usually predates that in white matter among MCI and AD. In short, increases in free-water and decreases in FA in gray matter are demonstrable beyond hippocampus and entorhinal cortex, and are associated with MCI and AD.

In the present study, higher amyloid SUVRs were associated with lower free-water in those with amyloid-negative status, while higher tau SUVRs were associated with higher free-water in those with amyloid-positive status. For amyloid, the results may correspond with the notion that amyloid deposits accumulate significantly in the initial progression of AD and eventually saturated at the later stage (Jack et al., 2010, 2013). The correlations were likely to be observed in the amyloid-negative subgroup where amyloid level continues to increase. However, readers must keep in mind that this finding is likely to be confounded with non-specific binding properties of amyloid PET imaging (Suppiah, Didier, & Vinjamuri, 2019) and sampling bias due to significant atrophy of the hippocampal region. Previous studies have shown close associ-

ations between white matter microstructural changes and amyloid accumulation in cognitively unimpaired and impaired subjects (Chao et al., 2013; Dong et al., 2020; Lee et al., 2020; Racine et al., 2014; Wen et al., 2021). These studies have reported that for MCI and AD subjects with a low level of amyloid burden (amyloid SUVR < 1.2–1.5), greater amyloid SUVRs were associated with more restricted diffusion in white matter. Conversely, for subjects who are in the later stages of AD or have a high global amyloid burden (amyloid SUVR > 1.5), greater amyloid SUVRs were associated with less restricted diffusion as reflected by increased MD and decreased FA (Collij et al., 2021; Dong et al., 2020; Racine et al., 2014; Wolf et al., 2015). The findings point to a nonlinear relationship between diffusion changes and amyloid deposition across different staging of AD. Our findings are in line with the previous evidence that increasing amyloid accumulation is associated with more restricted diffusion in those with lower global amyloid level (amyloid negative subgroup). Note that previous studies used global amyloid SUVRs to quantify amyloid burden, whereas in this paper regional SUVRs and diffusion measures were extracted from the same ROIs for each subject, offering a more direct regional examination of the relationship between the 2 measures. It is likely that higher extracellular amyloid plaques create hindrance and restriction of water movement, resulting in more restricted diffusion, which corresponds to lower free-water. Restrictions in extracellular water movement can also be caused by glial proliferation and activation of microglia and astrocytes, also prominent in AD pathology

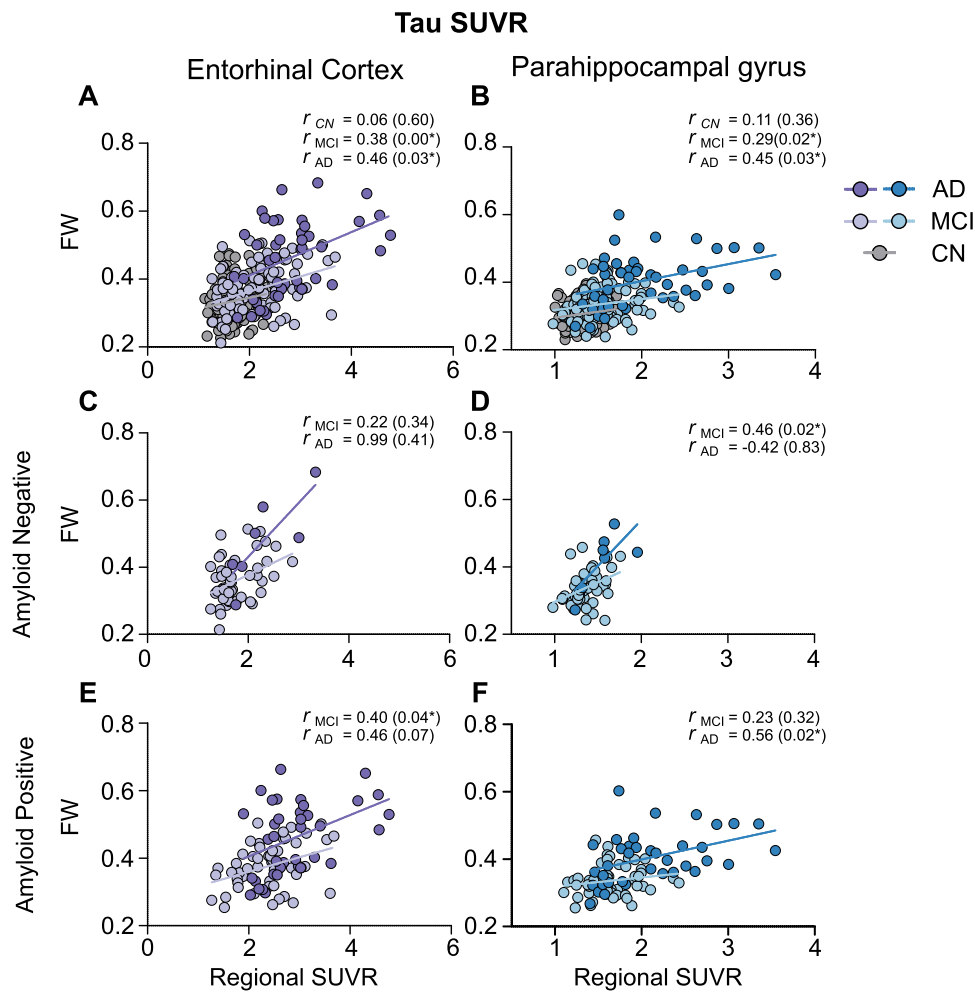


Fig. 4. Partial correlation analyses of free-water values with regional tau SUVRs in the entorhinal cortex (A,C,E) and the parahippocampus (B,D,E) for the CN, MCI, and the AD group. Figure C and D (second row) highlight the data from the MCI and the AD subjects who had amyloid-negative status. Figure D and F highlight the data from the MCI and the AD who had amyloid-positive status. * $p < 0.05$ after FDR correction.

(Ahmad et al., 2019; Heneka et al., 2015; Kaur et al., 2019; Mueggler et al., 2004; Rodriguez-Vieitez et al., 2016). In addition, we also observed a paradoxical finding that for the hippocampus ROI, the amyloid SUVRs were significantly lower in the AD and MCI groups compared to the control group. This result may have been due to the significant hippocampal atrophy in the MCI and AD groups. The lost neurons were likely to result from a higher level of amyloid deposits between neurons that with their absence, a smaller anatomical regions was sampled, which may bias the result (Hsu et al., 2015; Kadowaki et al., 2005). For tau deposition, an increasing in tau SUVRs was associated with increasing free-water regardless of amyloid status. Tau deposition has been associated with greater MD and lower FA in white matter regions including the hippocampal cingulum tract, and the posterior cingulum in preclinical AD (Pereira et al., 2019), MCI (Wen et al., 2021) and AD (Binette et al., 2021). Here, we replicate prior studies by showing a similar relationship between free-water and tau SUVRs and extend the result to gray matter brain regions. Intracellular tau protein deposition, which are thought to be responsible for neuronal loss (Gomez-Isla et al., 1997; Giannakopoulos et al., 2003) and axonal degeneration (de Calignon et al., 2012), are closely associated with macrostructural atrophy (Deture & Dickson, 2019). Cellular atrophy results in the breakdown of microstructural barriers such as myelin cell membranes and intracellular organelles that would nor-

mally restrict water molecule motion, leading to greater free-water diffusion (Montal et al., 2018; Weston et al., 2015).

Interpretation of diffusion measure change can be complicated as it interacts with multiple tissue changes and dynamic courses of inflammation, axonal swelling, and myelin loss, each with different cellular responses associated with distinct or overlapping diffusivity profiles (Winklewski et al., 2018). Nevertheless, a growing number of diffusion studies across the spectrum of AD severity have shown converging results of nonlinear patterns of diffusion changes in cognitively normal but amyloid positive individuals (Collij et al., 2021; Montal et al., 2018). These studies have suggested that in an early stage of the disease, acute glial swelling and glial activation lead to more diffusion barriers whereas in later AD stage, cellular barrier breakdown associated with axonal degeneration is likely to increase MD and free-water. Delineating microstructural alterations accompanying cellular pathology in AD improves our understanding of disease progression and the ability to better assess treatment efficacy. Future longitudinal studies are warranted to validate these relationships.

We found that when predicting subjects' MMSE scores 2 years later, the model including diffusion measures (FW & FA) and follow-up time achieved the highest r-squared predictive performance. Previous studies using diffusion measures have shown high classification accuracy (> 80%) in separating AD from normal

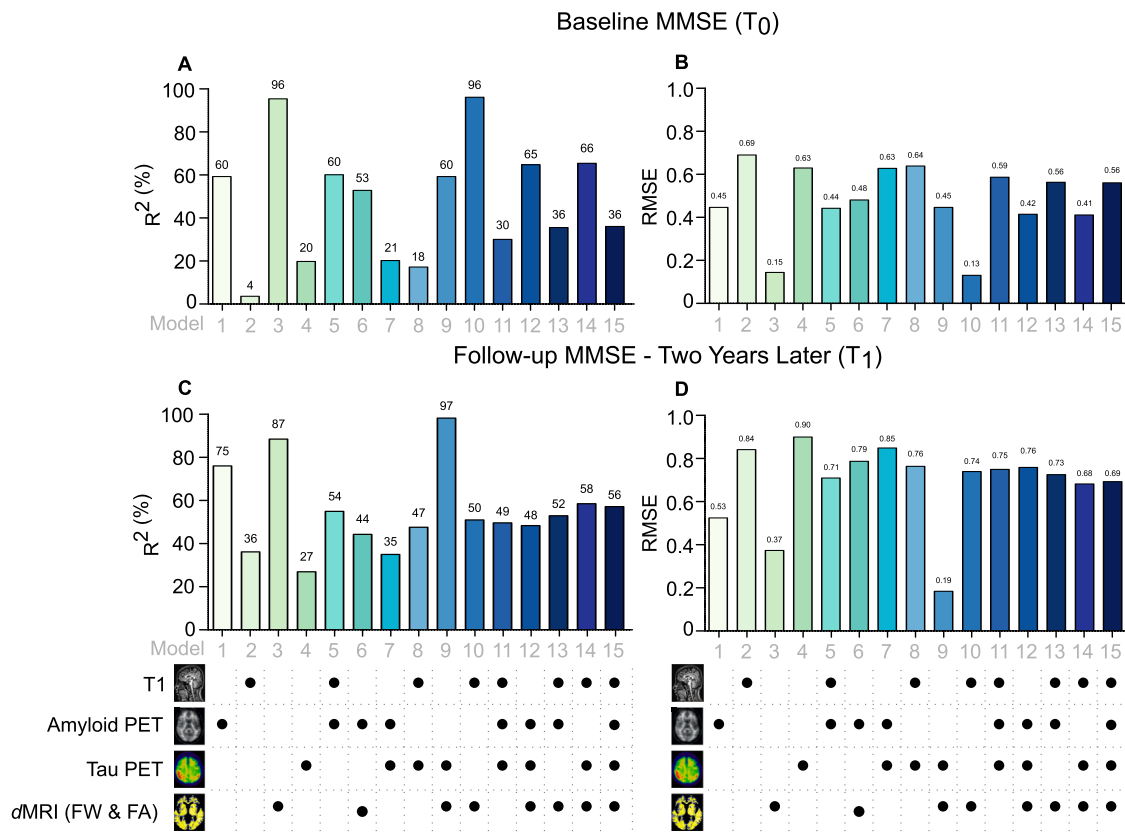


Fig. 5. The r-squared values and the root-mean-square error (RMSE) of different combinations of imaging modalities in predicting MMSE scores for the MCI subjects at (A, B) baseline (T₀) and (C, D) 2 years later (T₁) using SVM regression. In the prediction of baseline MMSE, age and sex were included as covariates in addition to imaging modalities, while in the prediction of follow-up MMSE, age, sex, and the time interval between baseline MMSE and MMSE 2 years later were included as covariates across all 15 models. Diffusion measures showed high predictive performances in predicting baseline MMSE ($R^2_{DTI} = 96\%$, $RMSE_{DTI} = 0.15$) and MMSE 2 years later ($R^2_{DTI} = 87\%$, $RMSE_{DTI} = 0.37$).

controls (Billeci et al., 2020). The use of the free-water model is more sensitive than a single-tensor model, and thus the current results could be due to the use of the more advanced and sensitive 2-compartment model (Ofori et al., 2017; Pasternak et al., 2018b). Moreover, we systematically evaluated the predictive performances of 4 types of brain imaging features individually and in their possible combinations on subjects' MMSE scores. Our novel finding is that when comparing each individual modality, the diffusion measure model showed the highest r squared value than any other imaging modality alone at each time point. Our data provide new evidence that diffusion changes in wide-spread gray matter regions are useful in predicting subjects' cognitive decline 2 years later. Advantages of diffusion MRI include lower costs compared to PET scans, no tracer required, close relationship with pathology, and a sensitive marker for early detection and improved diagnosis in early disease-state before conventional volumetric changes take place (Jack et al., 2010; Lee et al., 2020; Ofori et al., 2019; Weston et al., 2015). The use of diffusion markers also adds convenience, as most patients undergo an MRI scan, and the sequences can be added to a standard clinical procedure. Microstructural changes in gray matter regions offer useful information in predicting cognitive decline and hold potential value for monitoring the progression of AD in MCI populations.

We next offer considerations on methodology and interpretation of the current findings. First, for a typical diffusion imaging acquisition, water molecules in the brain are expected to have a mean displacement on the order of 5–10 micrometers (Pasternak et al., 2009), whereas the collected diffusion images are typically at a resolution of 1–1.5 mm (1000–1500 micrometers).

Resolution of PET images is even lower (~2mm), and the average size of a cell body ranges from 4 to 100 micrometers in diameter. Therefore, readers should interpret the findings across different imaging modalities with caution, especially when inferring conclusions at the cellular level. Second, not all of our MCI and AD cohort were amyloid-positive therefore we cannot exclude the possibilities that other proteinopathies may have confounded the result. Third, due to the unavailability of partial-volume-corrected amyloid SUVR on the ADNI website, additional sensitivity analyses were conducted using amyloid SUVRs normalized by the whole cerebellum, brainstem/pons, and eroded subcortical white matter, which mitigates the influence of partial volume effects (Wang et al., 2021). Significant associations between FW and amyloid SUVRs in the entorhinal cortex and hippocampus remain unchanged (Supplementary Fig. 1). One of the weaknesses of this work is that we did not use a composite cognitive score as our outcome measures such as ADNI-MEM and ADNI-EF (Crane et al., 2012). The study has shown these scores are more sensitive to cognitive decline and are better at predicting conversion from MCI to AD. Future studies, especially with longitudinal design should include these standardized composite scores.

5. Conclusions

Disruption of diffusion in the gray matter characterized by increased free-water and decreased FA across Braak stages was evident in individuals with MCI and AD. Increasing regional amyloid burden was associated with restricted diffusion when global amyloid level was low, while increasing regional tau burden was

associated with less restriction regardless of amyloid status. Diffusion measures from widespread brain regions was able to predict subjects' cognitive function at baseline and 2 years later with high predictive performances as compared to using T1, amyloid PET, or tau PET alone. Diffusion measures should be considered for predicting cognitive decline when amyloid/tau PET is not available or is too expensive.

Acknowledgements

We are grateful for the continued support from the 1Florida Alzheimer's Disease Research Center (ADRC) (NIH P30AG066506). Data collection and sharing for this project was funded by the Alzheimer's Disease Neuroimaging Initiative (ADNI) (National Institutes of Health Grant U01 AG024904) and DOD ADNI (Department of Defense award number W81XWH-12-2-0012). The support of the NSF grant CNS-1920182 is greatly appreciated. Fang is supported by the National Science Foundation under Grant No. (NSF 1908299). ADNI is funded by the National Institute on Aging, the National Institute of Biomedical Imaging and Bioengineering, and through generous contributions from the following: AbbVie, Alzheimer's Association; Alzheimer's Drug Discovery Foundation; Araclon Biotech; BioClinica, Inc.; Biogen; Bristol-Myers Squibb Company; CereSpir, Inc.; Cogstate; Eisai Inc.; Elan Pharmaceuticals, Inc.; Eli Lilly and Company; EuroImmun; F. Hoffmann-La Roche Ltd and its affiliated company Genentech, Inc.; Fujirebio; GE Healthcare; IXICO Ltd.; Janssen Alzheimer Immunotherapy Research & Development, LLC.; Johnson & Johnson Pharmaceutical Research & Development LLC.; Lumosity; Lundbeck; Merck & Co., Inc.; Meso Scale Diagnostics, LLC.; NeuroRx Research; Neurotrack Technologies; Novartis Pharmaceuticals Corporation; Pfizer Inc.; Piramal Imaging; Servier; Takeda Pharmaceutical Company; and Transition Therapeutics. The Canadian Institutes of Health Research is providing funds to support ADNI clinical sites in Canada. Private sector contributions are facilitated by the Foundation for the National Institutes of Health (www.fnih.org). The grantee organization is the Northern California Institute for Research and Education, and the study is coordinated by the Alzheimer's Therapeutic Research Institute at the University of Southern California. ADNI data are disseminated by the Laboratory for Neuro Imaging at the University of Southern California.

Declaration of Competing Interest

The authors declare no competing financial interests.

Supplementary materials

Supplementary material associated with this article can be found, in the online version, at doi:[10.1016/j.neurobiolaging.2022.10.013](https://doi.org/10.1016/j.neurobiolaging.2022.10.013).

References

- Ahmad, M.H., Fatima, M., Mondal, A.C., 2019. Influence of microglia and astrocyte activation in the neuroinflammatory pathogenesis of Alzheimer's disease: rational insights for the therapeutic approaches. *J Clin Neurosci* 59, 6–11. doi:[10.1016/j.jocn.2018.10.034](https://doi.org/10.1016/j.jocn.2018.10.034).
- Alzheimer's Association, 2021. 2021 Alzheimer's disease facts and figures. *Alzheimer's Dement* 17, 5. doi:[10.1002/alz.12328](https://doi.org/10.1002/alz.12328).
- Archer, D.B., Coombes, S.A., McFarland, N.R., DeKosky, S.T., Vaillancourt, D.E., 2019a. Development of a transcallosal tractography template and its application to dementia. *NeuroImage* 200, 302–312. doi:[10.1016/j.neuroimage.2019.06.065](https://doi.org/10.1016/j.neuroimage.2019.06.065).
- Archer, D.B., Coombes, S.A., McFarland, N.R., DeKosky, S.T., Vaillancourt, D.E., 2019b. Development of a transcallosal tractography template and its application to dementia. *NeuroImage* 200, 302–312. doi:[10.1016/j.neuroimage.2019.06.065](https://doi.org/10.1016/j.neuroimage.2019.06.065).
- Baker, S.L., Lockhart, S.N., Price, J.C., He, M., Huesman, R.H., Schonhaut, D., Faria, J., Rabinovici, G., Jagust, W.J., 2017. Reference tissue-based kinetic evaluation of 18F-AV-1451 for tau imaging. *J Nucl Med* 58, 332–338. doi:[10.2967/jnumed.116.175273](https://doi.org/10.2967/jnumed.116.175273).
- Baker, S.L., Maass, A., Jagust, W.J., 2017. Considerations and code for partial volume correcting [18F]-AV-1451 tau PET data. *Data Brief* 15, 648–657. doi:[10.1016/j.dib.2017.10.024](https://doi.org/10.1016/j.dib.2017.10.024).
- Bejanin, A., Schonhaut, D.R., La Joie, R., Kramer, J.H., Baker, S.L., Sosa, N., Ayakta, N., Cantwell, A., Janabi, M., Lauriola, M., O'Neil, J.P., Gorno-Tempini, M.L., Miller, Z.A., Rosen, H.J., Miller, B.L., Jagust, W.J., Rabinovici, G.D., 2017. Tau pathology and neurodegeneration contribute to cognitive impairment in Alzheimer's disease. *Brain* 140, 3286–3300. doi:[10.1093/brain/awx243](https://doi.org/10.1093/brain/awx243).
- Benjamini, Y., Hochberg, Y., 1995. Controlling the false discovery rate: a practical and powerful approach to multiple testing. *J. R. Stat. Soc., B: Stat. Methodol.* 57, 289–300. doi:[10.2307/2346101](https://doi.org/10.2307/2346101).
- Billeci, L., Badolato, A., Bachi, L., Tonacci, A., 2020. Machine learning for the classification of alzheimer's disease and its prodromal stage using brain diffusion tensor imaging data: A systematic review. *Processes* 8 (9). doi:[10.3390/pr8091071](https://doi.org/10.3390/pr8091071).
- Binette, A.P., Theaud, G., Rheault, F., Roy, M., Collins, D.L., Levin, J., Mori, H., Lee, J.H., Farlow, M.R., Schofield, P., Chhatwal, J.P., Masters, C.L., Benzinger, T., Morris, J., Bateman, R., Breitner, J.C.S., Poirier, J., Gonneaud, J., Descoteaux, M., Villeneuve, S., 2021. Bundle-specific associations between white matter microstructure and Ab and tau pathology in preclinical Alzheimer's disease. *eLife* 10, 1–28. doi:[10.7554/eLife.62929](https://doi.org/10.7554/eLife.62929).
- Braak, H., Braak, E., 1991. Neuropathological staging of Alzheimer-related changes. *Acta Neuropathologica* 82, 239–259. doi:[10.1007/BF00395630](https://doi.org/10.1007/BF00395630).
- Buckner, R.L., Head, D., Parker, J., Fotenos, A.F., Maris, J.C., Snyder, A.Z., 2004. A unified approach for morphometric and functional data analysis in young, old, and demented adults using automated atlas-based head size normalization: Reliability and validation against manual measurement of total intracranial volume. *NeuroImage* 23, 724–738. doi:[10.1016/j.neuroimage.2004.06.018](https://doi.org/10.1016/j.neuroimage.2004.06.018).
- Chao, L.L., DeCarli, C., Kriger, S., Truran, D., Zhang, Y., Laxamana, J., Villeneuve, S., Jagust, W.J., Sanossian, N., Mack, W.J., Chui, H.C., Weiner, M.W., 2013. Associations between white matter hyperintensities and β amyloid on integrity of projection, association, and limbic fiber tracts measured with diffusion tensor MRI. *PLoS ONE* 8. doi:[10.1371/journal.pone.0065175](https://doi.org/10.1371/journal.pone.0065175).
- Choo, I.H., Lee, D.Y., Oh, J.S., Lee, J.S., Lee, D.S., Song, I.C., Youn, J.C., Kim, S.G., Kim, K.W., Jhoo, J.H., Woo, J.L., 2010. Posterior cingulate cortex atrophy and regional cingulum disruption in mild cognitive impairment and Alzheimer's disease. *Neurobiol Aging* 31, 772–779. doi:[10.1016/j.neurobiolaging.2008.06.015](https://doi.org/10.1016/j.neurobiolaging.2008.06.015).
- Collij, L.E., Ingala, S., Top, H., Wottschel, V., Stickney, K.E., Tomassen, J., Konijnenberg, E., Kate, M.Ten, Sudre, C., Alves, I.L., Yaqub, M.M., Wink, A.M., Van 't Ent, D., Scheltens, P., van Berckel, B.N.M., Visser, P.J., Barkhof, F., Den Braber, A., 2021. White matter microstructure disruption in early stage amyloid pathology. *Alzheimer's Dement (Amst)* 13, 1–9. doi:[10.1002/dad2.12124](https://doi.org/10.1002/dad2.12124).
- Crane, P.K., Carle, A., Gibbons, L.E., Insel, P., Mackin, R.S., Gross, A., Mungas, D., 2012. Development and assessment of a composite score for memory in the Alzheimer's Disease Neuroimaging Initiative (ADNI). *Brain Imaging and Behavior* 6 (4), 502–516. doi:[10.1007/s11682-012-9186-z](https://doi.org/10.1007/s11682-012-9186-z).
- De Calignon, A., Polydoro, M., Suárez-Calvet, M., Williams, C., Adamowicz, D.H., Kopeikina, K.J., Hyman, B.T., 2012. Propagation of Tau Pathology in a Model of Early Alzheimer's Disease. *Neuron* 73 (4), 685–697. doi:[10.1016/j.neuron.2011.11.033](https://doi.org/10.1016/j.neuron.2011.11.033).
- Desikan, R.S., Ségonne, F., Fischl, B., Quinn, B.T., Dickerson, B.C., Blacker, D., Buckner, R.L., Dale, A.M., Maguire, R.P., Hyman, B.T., Albert, M.S., Killiany, R.J., 2006. An automated labeling system for subdividing the human cerebral cortex on MRI scans into gyral based regions of interest. *NeuroImage* 31, 968–980. doi:[10.1016/j.neuroimage.2006.01.021](https://doi.org/10.1016/j.neuroimage.2006.01.021).
- Deture, M.A., Dickson, D.W., 2019. The neuropathological diagnosis of Alzheimer's disease. *Mol. Neurodegener.* 14, 1–18. doi:[10.1186/s13024-019-0333-5](https://doi.org/10.1186/s13024-019-0333-5).
- Dong, J.W., Jelescu, I.O., Ades-Aron, B., Novikov, D.S., Friedman, K., Babb, J.S., Osorio, R.S., Galvin, J.E., Shepherd, T.M., Fieremans, E., 2020. Diffusion MRI biomarkers of white matter microstructure vary nonmonotonically with increasing cerebral amyloid deposition. *Neurobiol Aging* 89, 118–128. doi:[10.1016/j.neurobiolaging.2020.01.009](https://doi.org/10.1016/j.neurobiolaging.2020.01.009).
- Fortin, J.P., Parker, D., Tunç, B., Watanabe, T., Elliott, M.A., Ruparel, K., Roalf, D.R., Satterthwaite, T.D., Gur, R.C., Gur, R.E., Schultz, R.T., Verma, R., Shinohara, R.T., 2017. Harmonization of multi-site diffusion tensor imaging data. *NeuroImage* 161, 149–170. doi:[10.1016/j.neuroimage.2017.08.047](https://doi.org/10.1016/j.neuroimage.2017.08.047).
- Giannakopoulos, P., Herrmann, F.R., Bussièr, T., Bouras, C., Kövari, E., Perl, D.P., Hof, P.R., 2003. Tangle and neuron numbers, but not amyloid load, predict cognitive status in Alzheimer's disease. *Neurology* 60 (9), 1495–1500. doi:[10.1212/01.WNL.0000063311.58879.01](https://doi.org/10.1212/01.WNL.0000063311.58879.01).
- Gomez-Isola, T., Hollister, R., West, H., Mui, S., Growdon, J.H., Petersen, R.C., Hyman, B.T., 1997. Neuronal loss correlates with but exceeds neurofibrillary tangles in Alzheimer's disease. *Ann Neurol* 41 (1), 17–24.
- Grueso, S., Viejo-Sobera, R., 2021. Machine learning methods for predicting progression from mild cognitive impairment to Alzheimer's disease dementia: a systematic review. *Alzheimer's Res Ther.* 13. doi:[10.1186/s13195-021-00900-w](https://doi.org/10.1186/s13195-021-00900-w).
- Heneka, M.T., Carson, M.J., Khoury, J.E., Landreth, G.E., Brosseron, F., Feinstein, D.L., Jacobs, A.H., Wyss-Coray, T., Vitorica, J., Ransohoff, R.M., Herrup, K., Frautschy, S.A., Finsen, B., Brown, G.C., Verkhratsky, A., Yamanaka, K., Koistinaho, J., Latz, E., Halle, A., ..., Kummer, M.P., 2015. Neuroinflammation in

- Alzheimer's disease. *Lancet Neurol.* 14, 388–405. doi:10.1016/S1474-4422(15)70016-5.
- Henf, J., Grothe, M.J., Brueggen, K., Teipel, S., Dyrba, M., 2018. Mean diffusivity in cortical gray matter in Alzheimer's disease: the importance of partial volume correction. *NeuroImage Clin.* 17, 579–586. doi:10.1016/j.nicl.2017.10.005.
- Hsu, P.J., Shou, H., Benzinger, T., Marcus, D., Durbin, T., Morris, J.C., Sheline, Y.L., 2015. Amyloid burden in cognitively normal elderly is associated with preferential hippocampal subfield volume loss. *J Alzheimers Dis* 45, 27–33. doi:10.3233/JAD-141743.
- Jack, C.R., Knopman, D.S., Jagust, W.J., Shaw, L.M., Aisen, P.S., Weiner, M.W., Petersen, R.C., Trojanowski, J.Q., 2010. Hypothetical model of dynamic biomarkers of the Alzheimer's pathological cascade. *Lancet Neurol* 9, 119–128. doi:10.1016/S1474-4422(09)70299-6.
- Jack, C.R., Wiste, H.J., Lesnick, T.G., Weigand, S.D., Knopman, D.S., Vemuri, P., Pankratz, V.S., Senjem, M.L., Gunter, J.L., Mielke, M.M., Lowe, V.J., Boeve, B.F., Petersen, R.C., 2013. Brain β -amyloid load approaches a plateau. *Neurology* 80, 890–896. doi:10.1212/WNL.0b013e3182840bbe.
- Jacobs, H.L.L., Van Boxtel, M.P.J., Gronenschild, E.H.B.M., Uylings, H.B.M., Jolles, J., Verhey, F.R.J., 2013. Decreased gray matter diffusivity: a potential early Alzheimer's disease biomarker? *Alzheimer's Dement.* 9, 93–97. doi:10.1016/j.jalz.2011.11.004.
- Jagust, W.J., Landau, S.M., Shaw, L.M., Trojanowski, J.Q., Koeppe, R.A., Reiman, E.M., Foster, N.L., Petersen, R.C., Weiner, M.W., Price, J.C., Mathis, C.A., 2009. Relationships between biomarkers in aging and dementia. *Neurology* 73, 1193–1199. doi:10.1212/WNL.0b013e3181bc010c.
- Johnson, W.E., Li, C., Rabinovic, A., 2007. Adjusting batch effects in microarray expression data using empirical Bayes methods. *Biostatistics* 8, 118–127. doi:10.1093/biostatistics/kxj037.
- Kadowaki, H., Nishitoh, H., Urano, F., Sadamitsu, C., Matsuzawa, A., Takeda, K., Matsutani, H., Yodoi, J., Urano, Y., Nagano, T., Ichijo, H., 2005. Amyloid β induces neuronal cell death through ROS-mediated ASK1 activation. *Cell Death Differ.* 12, 19–24. doi:10.1038/sj.cdd.4401528.
- Kaur, D., Sharma, V., Deshmukh, R., 2019. Activation of microglia and astrocytes: a roadway to neuroinflammation and Alzheimer's disease. *Inflammopharmacology* 27, 663–677. doi:10.1007/s10787-019-00580-x.
- Lee, P., Kim, H.R., Jeong, Y., 2020. Detection of gray matter microstructural changes in Alzheimer's disease continuum using fiber orientation. *BMC Neurol.* 20, 1–10. doi:10.1186/s12883-020-01939-2.
- Leemans, A., Jones, D.K., 2009. The B-matrix must be rotated when correcting for subject motion in DTI data. *Magn Reson Med.* 61, 1336–1349. doi:10.1002/mrm.21890.
- Liu, Y., Spulber, G., Lehtimäki, K.K., Könönen, M., Hallikainen, I., Gröhn, H., Kivipelto, M., Hallikainen, M., Vanninen, R., Soininen, H., 2011. Diffusion imaging changes in grey matter in Alzheimer's disease: a potential marker of early neurodegeneration. *Neurobiol Aging* 32, 1558–1571. doi:10.1016/j.neurobiolaging.2009.10.006.
- Lo Buono, V., Palmeri, R., Corallo, F., Allone, C., Pria, D., Bramanti, P., Marino, S., 2020. Diffusion tensor imaging of white matter degeneration in early stage of Alzheimer's disease: a review. *Internat J Neurosci.* 130, 243–250. doi:10.1080/00207454.2019.1667798.
- Maass, A., Landau, S., Horng, A., Lockhart, S.N., Rabinovici, G.D., Jagust, W.J., Baker, S.L., La Joie, R., 2017. Comparison of multiple tau-PET measures as biomarkers in aging and Alzheimer's disease. *NeuroImage* 157, 448–463. doi:10.1016/j.neuroimage.2017.05.058.
- Montal, V., Vilaplana, E., Alcolea, D., Pegueroles, J., Pasternak, O., González-Ortiz, S., Clarimón, J., Carmona-Iragui, M., Illán-Gala, I., Morenas-Rodríguez, E., Ribosa-Nogué, R., Sala, I., Sánchez-Saudinós, M.B., García-Sebastian, M., Villanúa, J., Izagirre, A., Estanga, A., Ecaz-Torres, M., Iriondo, A., ..., Fortea, J., 2018. Cortical microstructural changes along the Alzheimer's disease continuum. *Alzheimer's Dement* 14, 340–351. doi:10.1016/j.jalz.2017.09.013.
- Mormino, E.C., Kluth, J.T., Madison, C.M., Rabinovici, G.D., Baker, S.L., Miller, B.L., Koeppe, R.A., Mathis, C.A., Weiner, M.W., Jagust, W.J., 2009. Episodic memory loss is related to hippocampal-mediated β -amyloid deposition in elderly subjects. *Brain* 132, 1310–1323. doi:10.1093/brain/awn320.
- Mueggler, T., Meyer-Luehmann, M., Rausch, M., Staufenbiel, M., Jucker, M., Rudin, M., 2004. Restricted diffusion in the brain of transgenic mice with cerebral amyloidosis. *Eur J Neurosci.* 20, 811–817. doi:10.1111/j.1460-9568.2004.03534.x.
- Ofori, E., Dekosky, S.T., Febo, M., Colon-perez, L., Chakrabarty, P., Duara, R., Adjouadi, M., Golde, T.E., Vaillancourt, D.E., Neuroimaging, D., 2019. Free-water imaging of the hippocampus is a sensitive marker of Alzheimer's disease. *NeuroImage Clin.* 24, 101985. doi:10.1016/j.nicl.2019.101985.
- Ofori, E., Krismer, F., Burciu, R.G., Pasternak, O., McCracken, J.L., Lewis, M.M., Du, G., McFarland, N.R., Okun, M.S., Poewe, W., Mueller, C., Gizewski, E.R., Schocke, M., Kremser, C., Li, H., Huang, X., Seppi, K., Vaillancourt, D.E., 2017. Free water improves detection of changes in the substantia nigra in parkinsonism: a multisite study. *Mov Disord.* 32, 1457–1464. doi:10.1002/mds.27100.
- Pasternak, O., Kelly, S., Sydnor, V.J., Shenton, M.E., 2018a. Advances in microstructural diffusion neuroimaging for psychiatric disorders. *NeuroImage* 182, 259–282. doi:10.1016/j.neuroimage.2018.04.051.
- Pasternak, O., Kelly, S., Sydnor, V.J., Shenton, M.E., 2018b. Advances in microstructural diffusion neuroimaging for psychiatric disorders. *NeuroImage.* 182, 259–282. doi:10.1016/j.neuroimage.2018.04.051.
- Pasternak, O., Sochen, N., Gur, Y., Intrator, N., Assaf, Y., 2009. Free water elimination and mapping from diffusion MRI. *Magn Reson Med.* 62, 717–730. doi:10.1002/mrm.22055.
- Pereira, J.B., Ossenkoppele, R., Palmqvist, S., Strandberg, T.O., Smith, R., Westman, E., Hansson, O., 2019. Amyloid and tau accumulate across distinct spatial networks and are differentially associated with brain connectivity. *ELife* 8, 1–25. doi:10.7554/eLife.50830.
- Pievani, M., Agosta, F., Pagani, E., Canu, E., Sala, S., Absinta, M., Geroldi, C., Ganzola, R., Frisoni, G.B., Filippi, M., 2010. Assessment of white matter tract damage in mild cognitive impairment and Alzheimer's disease. *Hum Brain Mapp.* 31, 1862–1875. doi:10.1002/hbm.20978.
- Racine, A.M., Adluru, N., Alexander, A.L., Christian, B.T., Okonkwo, O.C., Oh, J., Cleary, C.A., Birdsill, A., Hillmer, A.T., Murali, D., Barnhart, T.E., Gallagher, C.L., Carlsson, C.M., Rowley, H.A., Dowling, N.M., Asthana, S., Sager, M.A., Bendlin, B.B., Johnson, S.C., 2014. Associations between white matter microstructure and amyloid burden in preclinical Alzheimer's disease: A multimodal imaging investigation. *NeuroImage Clin.* 4, 604–614. doi:10.1016/j.nicl.2014.02.001.
- Rodriguez-Vieitez, E., Saint-Aubert, L., Carter, S.F., Almkvist, O., Farid, K., Schöll, M., Chiotis, K., Thordardottir, S., Graff, C., Wall, A., Långström, B., Nordberg, A., 2016. Diverging longitudinal changes in astrogliosis and amyloid PET in autosomal dominant Alzheimer's disease. *Brain* 139, 922–936. doi:10.1093/brain/aww404.
- Scola, E., Bozzali, M., Agosta, F., Magnani, G., Franceschi, M., Sormani, M.P., Cercignani, M., Pagani, E., Falautano, M., Filippi, M., Falini, A., 2010. A diffusion tensor MRI study of patients with MCI and AD with a 2-year clinical follow-up. *J Neurol Neurosurg Psychiatry* 81, 798–805. doi:10.1136/jnnp.2009.189639.
- Smith, S.M., Jenkinson, M., Woolrich, M.W., Beckmann, C.F., Behrens, T.E.J., Johansen-Berg, H., Bannister, P.R., De Luca, M., Drobnjak, I., Flitney, D.E., Niazy, R.K., Saunders, J., Vickers, J., Zhang, Y., De Stefano, N., Brady, J.M., Matthews, P.M., 2004. Advances in functional and structural MR image analysis and implementation as FSL. *NeuroImage* 23 (SUPPL. 1), 208–219. doi:10.1016/j.neuroimage.2004.07.051.
- Suppiah, S., Didier, M.A., Vinjamuri, S., 2019. The who, when, why, and how of PET amyloid imaging in management of Alzheimer's disease—review of literature and interesting images. *Diagnostics* 9 (2). doi:10.3390/diagnostics9020065.
- Tabarestani, S., Aghilii, M., Eslami, M., Cabrero, M., Barreto, A., Rishe, N., Curiel, R.E., Loewenstein, D., Duara, R., Adjouadi, M., 2020. A distributed multitask multimodal approach for the prediction of Alzheimer's disease in a longitudinal study. *NeuroImage* 206, 116317. doi:10.1016/j.neuroimage.2019.116317.
- Thal, D.R., Rüb, U., Orantes, M., Braak, H., 2002. Phases of A β -deposition in the human brain and its relevance for the development of AD. *Neurology* 58, 1791–1800. doi:10.1212/WNL.58.12.1791.
- Veitch, D.P., Weiner, M.W., Aisen, P.S., Beckett, L.A., Cairns, N.J., Green, R.C., Harvey, D., Jack, C.R., Jagust, W., Morris, J.C., Petersen, R.C., Saykin, A.J., Shaw, L.M., Toga, A.W., Trojanowski, J.Q., 2019. Understanding disease progression and improving Alzheimer's disease clinical trials: recent highlights from the Alzheimer's Disease Neuroimaging Initiative. *Alzheimer's Dement.* 15, 106–152. doi:10.1016/j.jalz.2018.08.005.
- Vemuri, P., Lowe, V.J., Knopman, D.S., Senjem, M.L., Kemp, B.J., Schwarz, C.G., Przybelski, S.A., Machulda, M.M., Petersen, R.C., Jack, C.R., 2017. Tau-PET uptake: Regional variation in average SUVR and impact of amyloid deposition. *Alzheimer's Dement (Amst)* 6, 21–30. doi:10.1016/j.dadm.2016.12.010.
- Wang, M., Yan, Z., Zhang, H., Lu, J., Li, L., Yu, J., Jiang, J., 2021. Parametric estimation of reference signal intensity in the quantification of amyloid-beta deposition: An 18F-AV-45 study. *Quantitative Imaging in Medicine and Surgery* 11 (1), 249–263. doi:10.21037/QIMS-20-110.
- Wen, Q., Risacher, S.L., Xie, L., Li, J., Harezlak, J., Farlow, M.R., Unverzagt, F.W., Gao, S., Apostolova, L.G., Saykin, A.J., Wu, Y.C., 2021. Tau-related white-matter alterations along spatially selective pathways. *NeuroImage* 226, 117560. doi:10.1016/j.neuroimage.2020.117560.
- Weston, P.S.J., Simpson, I.J.A., Ryan, N.S., Ourselin, S., Fox, N.C., 2015. Diffusion imaging changes in grey matter in Alzheimer's disease: a potential marker of early neurodegeneration. *Alzheimer's Res Ther.* 7, 1–8. doi:10.1186/s13195-015-0132-3.
- Winkiewicz, P.J., Sabisz, A., Naumczyk, P., Jodzio, K., Szurowska, E., Szarmach, A., 2018. Understanding the physiopathology behind axial and radial diffusivity changes—what do we know? *Front Neurol.* 9. doi:10.3389/fneur.2018.00092.
- Wolf, D., Fischer, F.U., Scheurich, A., Fellgiebel, A., 2015. Non-linear association between cerebral amyloid deposition and white matter microstructure in cognitively healthy older adults. *J Alzheimers Dis.* 47, 117–127. doi:10.3233/JAD-150049.